NANO LETTERS

pubs.acs.org/NanoLett

Letter

Nanoengineered Spintronic-Metasurface Terahertz Emitters Enable Beam Steering and Full Polarization Control

Shunjia Wang, Wentao Qin, Sheng Zhang, Yuchen Lou, Changqin Liu, Tong Wu, Qiong He, Chuanshan Tian, Lei Zhou, Yizheng Wu,* and Zhensheng Tao*

Cite This: *Nano Lett.* 2022, 22, 10111−10119

Read Online

ACCESS | Metrics & More | Article Recommendations | Supporting Information

ABSTRACT: The demand for emerging applications at the terahertz frequencies motivates the development of novel and multifunctional devices for the generation and manipulation of terahertz waves. In this work, we report the realization of multifunctional spintronic-metasurface emitters, which allow simultaneous beam-steering and full polarization control over a broadband terahertz beam. This is achieved through engineering individual meta-atoms with nanoscale magnetic heterostructures and, thus, implementing microscopical control over the laser-induced spin and charge dynamics. By arranging the spintronic meta-atoms in the metagrating geometry, the generated terahertz beam can be flexibly steered in space between different orders of diffraction. Furthermore, we demonstrate a simultaneous control over the terahertz polarization states at different emission angles and show that the two control capabilities are mutually independent of each other. The nanoengineered multifunctional terahertz emitter demonstrated in this work can provide a solution to the challenge associated with a growing variety of applications of terahertz technology.

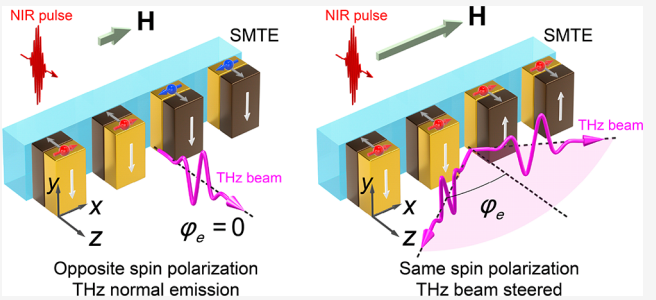

KEYWORDS: *Terahertz (THz), Spintronic nanotechnology, Metasurface, Light-wave manipulation*

The generation and manipulation of broadband terahertz radiation have attracted widespread attention because it can be used for a variety of applications including biomedical imaging and spectroscopy,[1−3] noninvasive inspection,[4,5] and high-speed wireless communications.[6,7] In addition, in the context of fundamental research, because the terahertz spectrum covers the eigenfrequencies of many low-energy excitations (phonons, magnons, and excitons) in condensed matters and vibrational modes of macromolecules, it is becoming increasingly useful in many different fields, enabling studies such as manipulation of spin waves,[8,9] coherent excitation of phonon[10,11] and exciton[12,13] dynamics, control of molecular rotation in the gas phase,[14] etc. To fully exploit these emerging applications, sophisticated control over the terahertz waveform is essential. In particular, the ability to steer the terahertz beam, while maintaining flexible and independent control over its polarization state, could open up new possibilities for many of the aforementioned applications. For example, when biological molecules and medicines are inspected by terahertz imaging and spectroscopy, the capability of generating chiral terahertz waves with opposite helicity could enable terahertz circular dichroism characterization, which is especially sensitive to the handedness of chiral macromolecules,[15] while the ability to steer the beam to an appropriate location could further make efficient scanning imaging possible.[16]

For beam-steering, different types of grating devices have been developed for the terahertz frequencies.[17−19] By implementing tunable materials such as graphene[20,21] and liquid crystals,[22,23] or cascaded metasurface geometry,[24] programmable control over the terahertz wavefront is also demonstrated. For polarization control, on the other hand, free-space terahertz elements including wire-grid polarizers,[25,26] waveplates,[27,28] and metasurfaces[29,30] have been designed. In particular, the terahertz metasurfaces have attracted increasing interest in recent years, because of their compactness, ease of fabrication, and unprecedented capability in controlling terahertz waveforms.[31−34] Although the capability of beam-steering and polarization control has been realized separately using these free-space elements, multifunctional control using a single device still remains challenging. In addition, such free-space manipulation of terahertz waves usually requires inserting optical elements in the beam path, and it encounters significant limitations related to low efficiency and narrow manipulation bandwidth. Therefore, it

Received: October 6, 2022
Revised: December 8, 2022
Published: December 13, 2022

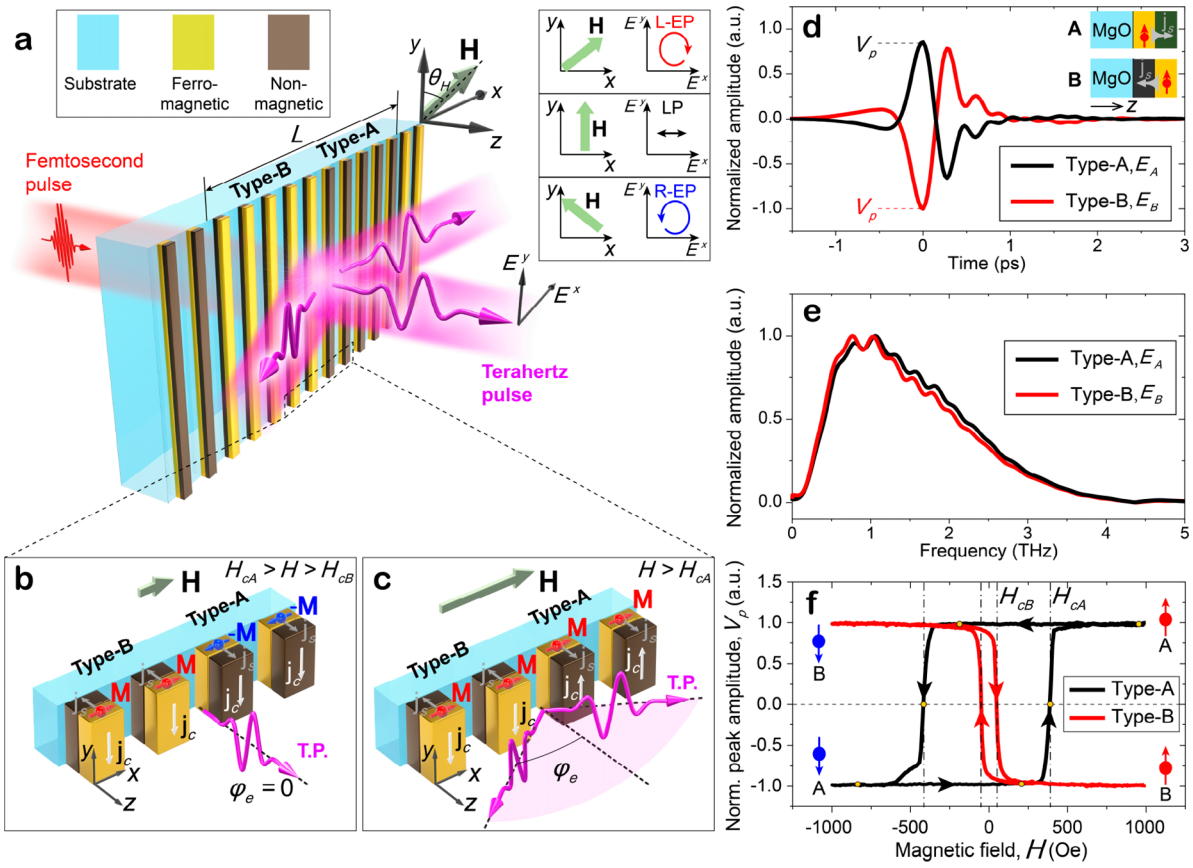

Figure 1. Beam-steering and polarization control with nanoengineered multifunctional SMTE. (a) Schematic of the SMTE device for the generation and manipulation of terahertz pulses (T.P.). An oriented external magnetic field (**H**) is applied in the $x-y$ plane to control the magnetization of the FM layers with a field angle of θ_H. Inset: The manipulation of the terahertz polarization state with the field angle. L-EP: Left elliptical polarization. R-EP: Right elliptical polarization. LP: Linear polarization. (b) The schematic of the FM-layer magnetization (**M**), the spin currents, and the charge currents in the type-A and -B heterostructures, when $H_{cA} > H > H_{cB}$. The terahertz pulse is emitted normal to the SMTE surface. (c) Same as part b but under a magnetic saturation field ($H > H_{cA}$). The terahertz pulses are emitted with an emission angle of φ_e in the $x-z$ plane. (d) Generation of short terahertz pulses from the type-A and -B thin films with the magnetic field strength H = 1000 Oe aligned in the x-direction. The peak field amplitude (V_p) is labeled. Inset: Illustration of the spin current flows in the type-A and -B heterostructures after laser excitation. (e) The terahertz spectra obtained by the Fourier transform of the transients in part d. (f) The hysteresis curves of V_p as a function of H measured on the type-A and -B thin films.

would be extremely attractive if we can directly combine efficient broadband terahertz emitters with the metasurface technology, which could give rise to compact and broadband terahertz sources with multifunctional and flexible control over different properties of a terahertz beam.

It is worth mentioning that there have been a few attempts using metasurfaces to manipulate terahertz waveforms directly during the generation process. For instance, by utilizing the optical rectification of a meta-atom, the pioneering work has demonstrated the generation of broadband terahertz waveforms through nonlinear metasurface devices.[35−38] It has been shown that, by appropriately designing the electromagnetic (EM) response of the meta-atoms, spatially separated circularly[39] and linearly[40] polarized terahertz beams can be generated and optically controlled. However, due to the low nonlinear coefficients of noble metals (typically gold) that make up the meta-atoms, the generation efficiency of these devices is usually limited. Furthermore, in the previous work, for generating one combination of the polarization and wavefront state of the output beam, it is often necessary to design and fabricate a specific metasurface structure.

In recent work, we proposed a novel spintronic-metasurface terahertz emitter (SMTE), which successfully combines the advantage of spintronic emitters for being ultra-broadband and efficient[41−43] and the powerful capability of metasurfaces for light-wave manipulation.[29,44,45] By controlling the magnetization of the ferromagnetic (FM) materials, and, hence, the EM response of the magnetic meta-atoms in the SMTE, the efficient and flexible control of the polarization state of the generated terahertz waves in a normal direction was demonstrated.[46] However, the demonstrated SMTE device was not multifunctional, and only the spatially anisotropic EM response of the individual meta-atoms was utilized. Taking advantage of the sophisticated modern spintronic nanotechnology,[47] it is possible to further engineer the collective response of the entire metasurface by controlling the microscopic spin and charge dynamics, which could greatly enrich the device functions. This advancement will be essential for realizing multifunctional SMTE devices, which can enable the direct generation and manipulation of terahertz fields with complex polarization textures in space[48] or in ultrashort temporal pulses.[49]

In this work, we close this gap by demonstrating the first multifunctional SMTE, which is able to generate broadband terahertz waves, while simultaneously realizing the beam-steering and polarization control of the terahertz radiation.

https://doi.org/10.1021/acs.nanolett.2c03906
Nano Lett. 2022, 22, 10111−10119

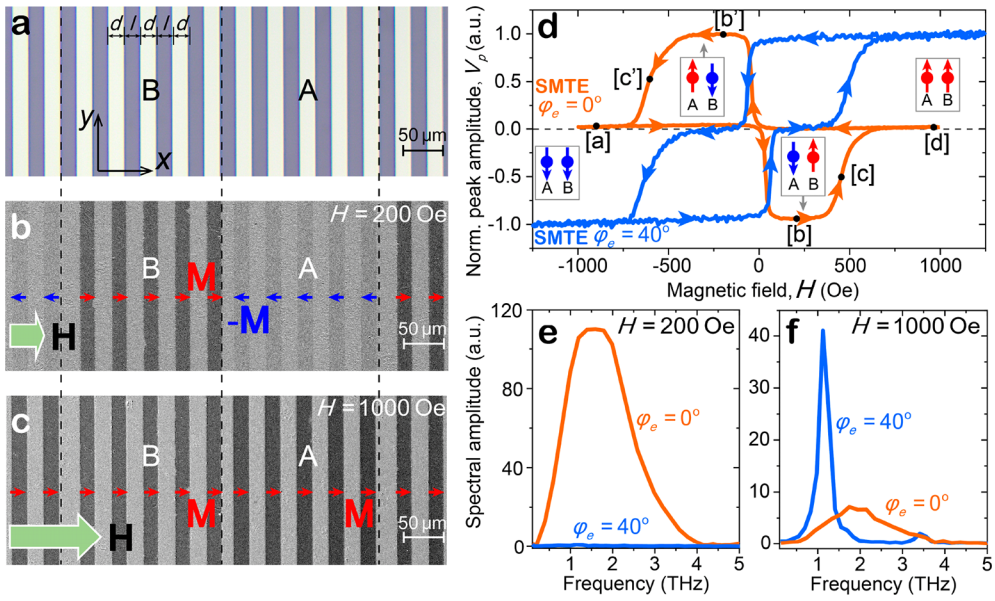

Figure 2. Hysteresis behaviors of the SMTE device. (a) The microscope image of the stripe-patterned metasurface. (b) The image obtained by the Kerr microscopy measurement under an external magnetic field of H = 200 Oe aligned along the +x-direction. The bright color of the stripes represents the magnetization (**M**) along the +x-direction, while the dark color represents **M** pointing to the −x-direction. (c) Same as part b but for H = 1000 Oe. (d) The hysteresis curves of V_p obtained from SMTE along two emission angles of φ_e = 0° and 40°. The same routes as in Figure 1f are labeled here, with the corresponding spin polarizations in the type-A and -B stripes. (e) The terahertz spectra measured at φ_e = 0° and 40° under H = 200 Oe. (f) Same as part e but for H = 1000 Oe.

This is achieved by engineering individual meta-atoms with different nanoscale magnetic heterostructures and making them possess distinct coercivity. Hence, the microscopic laser-induced spin and charge dynamics can be precisely controlled by an external magnetic field, leading to the tunable functionality of a single SMTE device. Here, we show that, by arranging the spintronic meta-atoms in a metagrating geometry and controlling the magnetic field strength, the terahertz beam can be flexibly steered in space between the different orders of diffraction. Furthermore, the full control of the polarization state of the generated terahertz waves is demonstrated for a wide range of emission angles, which is enabled by the geometric confinement effect.[46] Our results show that, by introducing modern spintronic nanotechnology into the design and fabrication of SMTE devices, we can realize many more different functions of SMTE, which could meet the challenges associated with the increasingly diverse applications of the terahertz technology.

The schematic of the SMTE for generating and controlling the terahertz waves is illustrated in Figure 1a. The SMTE device is excited by femtosecond laser pulses with a pulse duration of ∼24 fs, a center wavelength of 1030 nm, and a repetition rate of 100 kHz. The excitation laser pulses are generated by high-quality pulse compression enabled by solitary beam propagation in periodic layered Kerr media.[50,51] The laser beam is normal incident from the substrate side onto the SMTE sample along the z-axis, with the beam radius ∼1.5 mm on the sample. The excitation pulse energy is ∼12 μJ. An external magnetic field (**H**) is applied in the x−y plane, which enables the control over the magnetization (**M**) of the ferromagnetic materials. The field angle θ_H is defined as the relative angle between **H** and the y-axis (see Figure 1a). The emitted terahertz waveforms are detected by a space-, polarization-, and time-resolved terahertz spectroscopy setup based on electro-optic sampling (EOS)[52,53] (see Supporting Information section S1).

The SMTE device is composed of nanometer-thick stripe-patterned ferromagnetic/nonmagnetic (FM/NM) heterostructures. As illustrated in Figure 1b and c, when the heterostructures are excited by femtosecond laser pulses, nonequilibrium spin-polarized electrons are generated in the FM layer and subsequently diffuse to the NM layer, resulting in a longitudinal spin current ($\mathbf{j}_s$).[54] Due to the inverse spin-Hall effect (ISHE), the spin current is further converted into a transverse charge current ($\mathbf{j}_c$), by $\mathbf{j}_c = \gamma \mathbf{j}_s \times \mathbf{M}/|\mathbf{M}|$, leading to broadband terahertz emission.[42] Here, γ is the spin-Hall angle of the NM material. To control the generated terahertz waves, we have fabricated two types of magnetic heterostructures in a single SMTE device: type-A FM/NM and type-B NM/FM (see Figure 1a−c), using the micro−nano processing technology. In both structures, the NM layer is a 3 nm Pt layer and the FM layer is a 1.5 nm Fe layer, but they are grown in reversed order. Therefore, after laser excitation, the spin currents ($\mathbf{j}_s$) flow in the opposite directions (+z-direction in the type-A structure and −z-direction in the type-B structure, Figure 1b and c). To further implement control over the FM-layer magnetization in different stripes, we have predeposited an antiferromagnetic (AFM) CoO (3 nm)/NiO (1.5 nm) layer in the type-A heterostructure. Therefore, the interfacial exchange interaction between the AFM and FM layers substantially increases the coercive field strength of the type-A structure.[55] The difference in thickness is then compensated by predepositing a 4 nm-thick Al_2O_3 layer in the type-B structure. The "lattice" of the metasurface is composed of these two types of stripes, periodically stacked along the x-axis. The stripe width is l = 20 μm, and the spacing is d = 20 μm. Each type of the heterostructures alternatively repeats n = 5 times in space, forming a "superlattice" with a lattice constant of $L = 2n$

https://doi.org/10.1021/acs.nanolett.2c03906
Nano Lett. 2022, 22, 10111−10119

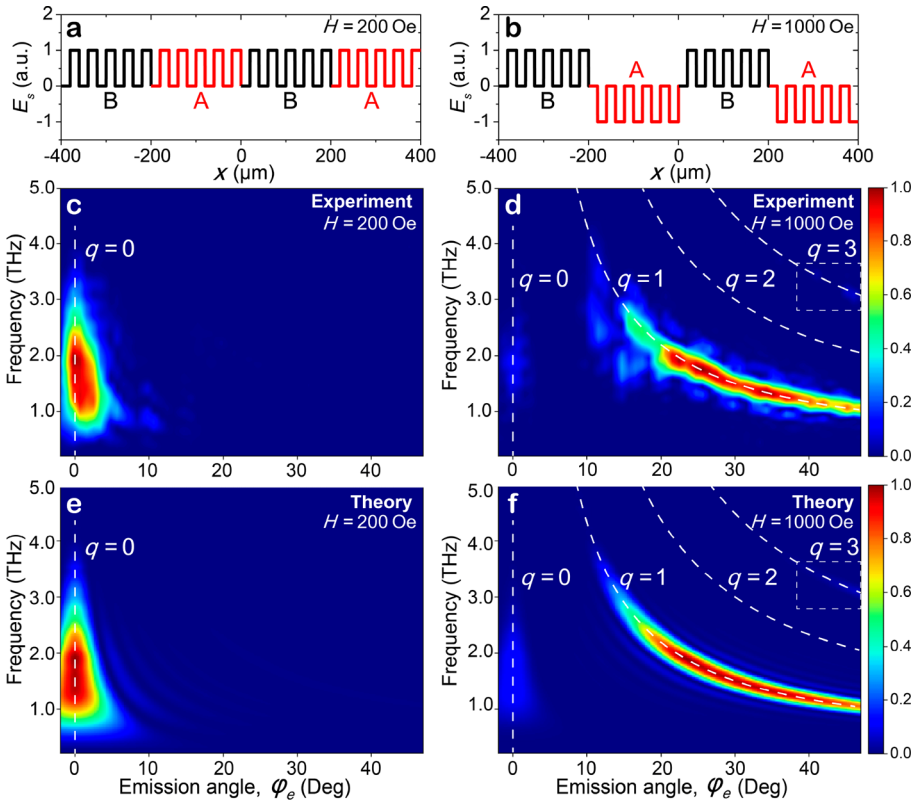

Figure 3. Beam-steering capability of the SMTE device. (a) The schematic of the local-field amplitude of E_s on the surface of SMTE when H = 200 Oe. (b) Same as part a but for H = 1000 Oe. (c) The experimentally measured spatio-spectral distribution of the terahertz wave amplitudes under H = 200 Oe, with a spectral range from 0.2 to 5.0 THz and an emission angle φ_e from −2° to 47°. (d) Same as part c but for H = 1000 Oe. The white dashed lines in parts c and d represent the spatial chirp of the terahertz waves at q = 0−3 diffraction orders. The q = 3 diffraction order is labeled by the square box. (e and f) The model results for H = 200 and 1000 Oe, respectively, in direct comparison with the experimental results in parts c and d.

× (l + d) = 400 μm (see Figure 1a). Details of sample fabrication are provided in Supporting Information section S2.

Here, we first calibrate the terahertz emission from the two different types of heterostructures. In Figure 1d, we plot the transients of the terahertz waves (E_A and E_B) generated by the homogeneous thin films. The magnetic field (**H**) saturates the sample magnetization (**M**) along the x-axis with a field strength H = 1000 Oe, where H denotes the strength of the magnetic field. Because the spin current $\mathbf{j}_s$ flows reversely along z in the two thin-film samples (inset of Figure 1d), E_A and E_B exhibit opposite polarities with an approximately equal field amplitude. The corresponding terahertz spectra are also identical, which can cover a broad frequency range of 0.1−4.5 THz (Figure 1e). In Figure 1f, we present the hysteresis curves of the type-A and -B thin films by plotting the normalized peak amplitudes (V_p) of the terahertz transients. The magnetic field **H** remains aligned along the x-axis. We find that the coercive field strength of the type-B heterostructure (H_{cB}) is ∼50 Oe, while that of the type-A structure (H_{cA}) is extensively increased to ∼380 Oe due to the interfacial exchange interaction between the AFM and the FM layer.[55]

Using the optical lithography and ion-beam etching (see Supporting Information section S2), we fabricate the SMTE device with the stripes that consist of the type-A and -B heterostructures (Figure 1a), and the two types of stripes can well preserve the difference in coercivity. The control over the magnetization of the individual meta-atoms can be clearly demonstrated by the Kerr microscopy measurements (see Supporting Information section S3). In Figure 2a−c, we present the microscopy images of the sample magnetization in a metasurface "superlattice" under different H. The magnetic field is first saturated along the $-x$ direction and then sweeps to the saturation along the $+x$ direction. During the sweeping, we find that the two types of stripes first possess opposite magnetization when H = 200 Oe (see Figure 2b) and then they are switched to align with each other when H is sufficiently high (e.g., H = 1000 Oe in Figure 2c).

The hysteresis curves of SMTE probed at the emission angles of φ_e = 0° and 40° are plotted in Figure 2d. Here, φ_e is the emission angle of the terahertz beams in the x−z plane (Figure 1c). For the angle-resolved measurements, the excitation laser beam remains normal incident to the SMTE sample, while the terahertz emission at different φ_e is exposed to the detection system by rotating the sample about the y-axis (see Supporting Information section S1). The normalized peak amplitudes (V_p) are plotted. By sweeping H following the [a] → [b] → [c] → [d] route, we observe sequential switch-on and -off of the terahertz emission along φ_e = 0°. This can be understood by the constructive and destructive interference of E_A and E_B, whose polarities can be switched by different H. Similar behaviors can be observed when H sweeps along the [d] → [b′] → [c′] → [a] route (Figure 2d), but the polarity of the terahertz wave is reversed. Also shown in Figure 2d, we observe that the off-axis terahertz radiation (e.g., φ_e = 40°) exhibits a complementary hysteresis behavior when compared to the normal emission (φ_e = 0°). The corresponding terahertz

https://doi.org/10.1021/acs.nanolett.2c03906
Nano Lett. 2022, 22, 10111−10119

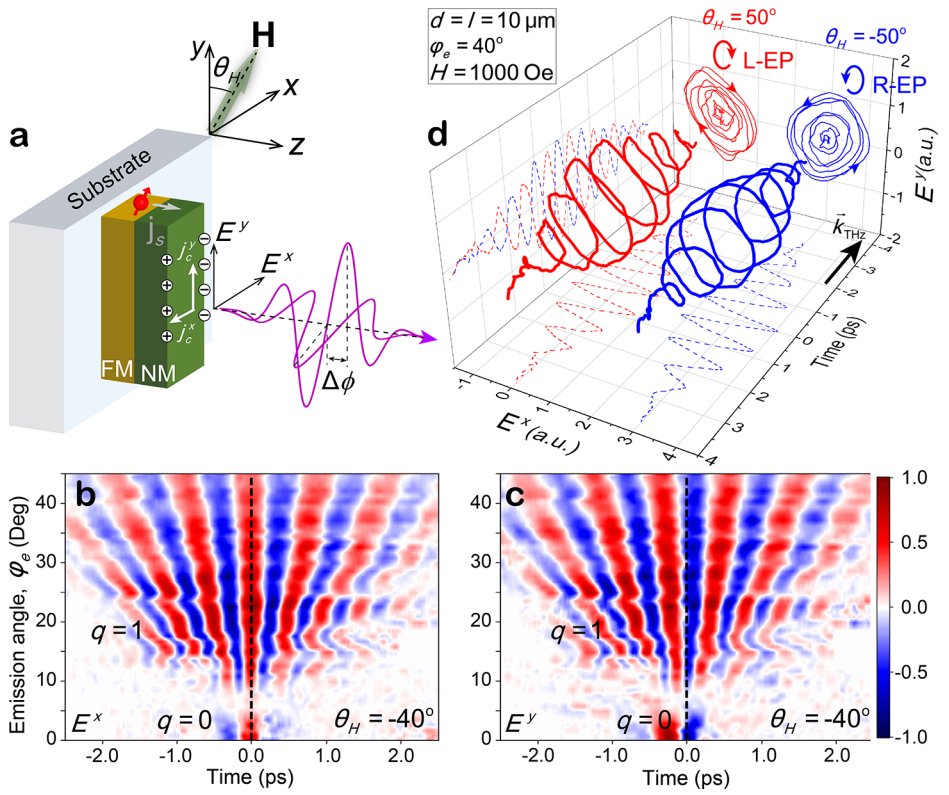

Figure 4. Polarization-control capability of the SMTE device. (a) The schematic of the geometric confinement effect in a single stripe of the heterostructure. The transverse charge current j_c^x is confined by the boundaries of the stripe which induces charge accumulation at the boundaries. The resultant capacitive effect leads to a relative phase shift $\Delta\phi$ between the E^y and E^x components of the generated terahertz wave. (b) The full measurement of the E^x temporal profiles of generated terahertz waves at the emission angle φ_e in the range from 0° to 45°. The magnetic field **H** is applied with $\theta_H = -40°$ and $H = 1000$ Oe. (c) Same condition as part b but for the E^y component. The time zeros are labeled by the black dashed lines in parts b and c. (d) The three-dimensional temporal profiles of the terahertz waveforms emitted at $\varphi_e = 40°$ under different field angles $\theta_H = -50°$ and 50°. The SMTE with the stripe width and spacing of $d = l = 10\ \mu m$ is chosen for higher ellipticity. Different helicities of the terahertz waves, left elliptical polarization (L-EP) and right elliptical polarization (R-EP), are labeled. The magnetic field strength is $H = 1000$ Oe.

spectra obtained at $\varphi_e = 0°$ and 40° are presented in Figure 2e and f for $H = 200$ and 1000 Oe, respectively. We observe that, for the off-axial terahertz wave, the spectral bandwidth is narrower and the center frequency is different compared to the normal emission (Figure 2e and f). This can be attributed to the spatial chirp induced by the metagrating (see below). These results clearly demonstrate the controllable beam-steering capability of SMTE.

The far-field terahertz wave (E_{far}) emitted at an angle of φ_e under a magnetic field strength of H is determined by the coherent summation of the terahertz waves emitted from all the stripes that compose the metasurface and are excited by the laser pulse. Hence, the spectral component with a terahertz angular frequency ω is given by

$$E_{far}(\omega, \varphi_e, H) = \int_{-\infty}^{\infty} E_s(\omega, x, H) e^{ik_x x}\, dx \quad (1)$$

where $E_s(\omega, x, H)$ is the terahertz radiation generated at the spatial position of x on the metasurface and $k_x = \frac{\omega \sin \varphi_e}{c}$ is the x-component of the terahertz wavevector, with c denoting the speed of light. Equation 1 simply corresponds to the spatial Fourier transform of $E_s(\omega, x, H)$. Because the waveforms of E_A and E_B are identical (Figure 1d), we can further decouple the terms of the oscillating electric fields. As a result, E_{far} is determined by the spatial distribution of the E_s amplitude (Figure 3a and b). Clearly, the stripe-patterned SMTE here works as a metagrating composed of the spintronic meta-atoms, with the periodicity Λ controllable by the external magnetic field.

In order to show the complete spatial and temporal profiles of the steered terahertz wave packet, we conduct scans of the terahertz waveforms in a wide emission angle (φ_e). As shown in Figure 3c, when $H = 200$ Oe and E_A and E_B have the same polarity (+1), we only observe the normal emission (zeroth order). With the metagrating periodicity $\Lambda = 40\ \mu m$ (Figure 3a), the first-order ($q = 1$) diffraction would appear at $k_x = \frac{2\pi}{\Lambda} \approx 0.157\ \mu m^{-1}$. This value is larger than the wavevector of a 5 THz EM wave, the upper frequency limit of the spectrum ($k \approx 0.105\ \mu m^{-1}$). Therefore, no terahertz emission at large angles can be observed. In stark contrast, when we increase H to 1000 Oe, since the E_A and E_B have the opposite polarities (±1), the destructive interference suppresses the emission of the $q = 0$ order. Meanwhile, the metagrating periodicity is changed to $\Lambda = 400\ \mu m$ (Figure 3b), which yields the $q = 1$ order wavevector of $k_x \approx 0.0157\ \mu m^{-1}$. The first-order metagrating diffraction leads to the spatial chirp of the terahertz waves by $\omega = \frac{c k_x}{\sin \varphi_e}$ (the white dashed lines in Figure 3d), which is in excellent agreement with our experimental results. Furthermore, we also observe a weak $q = 3$ order emission at larger emission angles, but its intensity is <12% of the $q = 1$ order (Figure 2f). Similar results would also be observed for $q = -1$ and -3 in the region where $\varphi_e < 0$. We note that the emission of the $q = \pm 2$

https://doi.org/10.1021/acs.nanolett.2c03906
Nano Lett. 2022, 22, 10111−10119

diffraction orders is forbidden here considering the symmetry of the metagrating; i.e., the superlattice possesses the mirror symmetry of the positive and negative polarities. In Figure 3e and f, we present the wave-propagation simulations, and the results exhibit excellent agreement with the experimental results. In the simulation, the finite spot size of the excitation laser, as well as the experimental terahertz spectrum, are considered (see Supporting Information section S6).

We note that our design principle is scalable and can be adapted to more complex beam-steering functions. For example, by introducing more spintronic meta-atoms with different strengths of coercivity, which can be realized by varying the thickness of the AFM layer,[55] our simulations show that the device can flexibly switch the terahertz beam in space between the $q = 0$, $q = \pm 1$, and $q = \pm 2$ orders controlled by the external magnetic field (see Supporting Information section S8). In addition, the intensity of the higher-order diffraction (e.g., $q = 3$) can be suppressed, enabling high-quality beam-steering. This can be realized by modulating the emission amplitudes from individual meta-atoms or by limiting the terahertz emission bandwidth (see Supporting Information section S7). The former can be achieved by precisely controlling the thickness of the FM or NM layer through the micro−nano processing technology.[43]

In Figure 4, we further demonstrate the full control of the terahertz polarization state. This is enabled by changing the field angle θ_H (inset of Figure 1a), which leads to the transverse geometric confinement on the laser-induced charge currents ($\mathbf{j}_c$),[46] as illustrated in Figure 4a (see Supporting Information section S5). In Figure 4b and c, we present the experimentally measured spatiotemporal structures of the E^x and E^y components at the field angle of $\theta_H = -40°$. The magnetic field strength is $H = 1000$ Oe, and the terahertz-field amplitudes are normalized at each φ_e for clearly presenting the phase difference. For simplicity, the time zero is taken as the symmetrical center of the E^x temporal profiles. The $q = 1$ order emission can be well observed ranging from $\varphi_e = 10°$ to 45°, and some weak leakage of the $q = 0$ order is found in the range of 0°−5°. Because of the spatial chirp of the $q = 1$ order, terahertz waves with higher frequency are emitted at smaller φ_e, which also yields a shorter pulse duration. When comparing the results in Figure 4b and c, a clear phase difference $\Delta\phi$ can be observed between the E^y and E^x components, which leads to the elliptically polarized (EP) terahertz waves. For $l = 20$ μm and $\theta_H = -40°$, $\Delta\phi$ is typically ∼2.0 rad over the 0.1−4.5 terahertz bandwidth, resulting in an overall ellipticity of $\varepsilon \sim 0.6$, consistent with the previous results.[46] The spatiotemporal results in Figure 4b and c can be well reproduced by the numerical simulations using the frequency-domain solver of COMSOL Multiphysics (see Supporting Information section S4). In Figure 4d, we present the full control of the polarization state of the generated terahertz wave along $\varphi_e = 50°$. The three-dimensional terahertz waveforms at different field angles θ_H and under $H = 1000$ Oe are presented. When $\theta_H = -50°$, the left-handed elliptically polarized (L-EP) terahertz waves can be generated, defined from the point of view of the receiver. By controlling θ_H, the ellipticity and handedness of the terahertz wave can be continuously tuned (see Supporting Information section S5). These results combined clearly demonstrate that the multifunctional device can provide full control of the terahertz polarization state over a wide range of emission angles.

In conclusion, we show the realization of the nano-engineered multifunctional SMTE device, which enables the generation of broadband terahertz waves, and meanwhile possesses beam-steering and polarization-control capabilities. The demonstrated capability could open up new applications in terahertz spectroscopy and imaging. Moreover, we believe that our prototype only shows the tip of the iceberg of the design principle. By further introducing different magnetic materials,[56] spintronic effects,[57,58] complex meta-atom designs,[29,45] and the laser-assisted magnetic-printing technology,[59] it has great potential to develop advanced multifunctional metasurface emitters that can realize complex terahertz waveforms, including terahertz vortex beams[48] and toroidal pulses.[49] Furthermore, the switching speed of the current device is limited by the use of a conventional electromagnet in our experiments. The switching speed can be significantly increased to the microsecond time scales by, for example, using an ac magnetic field.[60]

■ ASSOCIATED CONTENT

Supporting Information

The Supporting Information is available free of charge at https://pubs.acs.org/doi/10.1021/acs.nanolett.2c03906.

Experimental setup, sample fabrication, COMSOL simulations, supplementary experimental results, wave-propagation simulations, suppression of higher-order diffraction, and extension of the beam-steering functionality (PDF)

■ AUTHOR INFORMATION

Corresponding Authors

Yizheng Wu − *State Key Laboratory of Surface Physics and Department of Physics, Fudan University, Shanghai 200433, China; Shanghai Research Center for Quantum Sciences, Fudan University, Shanghai 200433, China;* orcid.org/0000-0002-9289-1271; Email: wuyizheng@fudan.edu.cn

Zhensheng Tao − *State Key Laboratory of Surface Physics and Department of Physics, Fudan University, Shanghai 200433, China; Key Laboratory of Micro and Nano Photonic Structures (MOE), Fudan University, Shanghai 200433, China;* orcid.org/0000-0002-8727-3719; Email: zhenshengtao@fudan.edu.cn

Authors

Shunjia Wang − *State Key Laboratory of Surface Physics and Department of Physics, Fudan University, Shanghai 200433, China; Key Laboratory of Micro and Nano Photonic Structures (MOE), Fudan University, Shanghai 200433, China*

Wentao Qin − *State Key Laboratory of Surface Physics and Department of Physics, Fudan University, Shanghai 200433, China; Shanghai Research Center for Quantum Sciences, Fudan University, Shanghai 200433, China*

Sheng Zhang − *State Key Laboratory of Surface Physics and Department of Physics, Fudan University, Shanghai 200433, China; Key Laboratory of Micro and Nano Photonic Structures (MOE), Fudan University, Shanghai 200433, China*

Yuchen Lou − *State Key Laboratory of Surface Physics and Department of Physics, Fudan University, Shanghai 200433, China; Key Laboratory of Micro and Nano Photonic*

Structures (MOE), Fudan University, Shanghai 200433, China

Changqin Liu − *State Key Laboratory of Surface Physics and Department of Physics, Fudan University, Shanghai 200433, China; Shanghai Research Center for Quantum Sciences, Fudan University, Shanghai 200433, China*

Tong Wu − *State Key Laboratory of Surface Physics and Department of Physics, Fudan University, Shanghai 200433, China; Shanghai Research Center for Quantum Sciences, Fudan University, Shanghai 200433, China*

Qiong He − *State Key Laboratory of Surface Physics and Department of Physics, Fudan University, Shanghai 200433, China; Key Laboratory of Micro and Nano Photonic Structures (MOE), Fudan University, Shanghai 200433, China*

Chuanshan Tian − *State Key Laboratory of Surface Physics and Department of Physics, Fudan University, Shanghai 200433, China; Key Laboratory of Micro and Nano Photonic Structures (MOE), Fudan University, Shanghai 200433, China;* orcid.org/0000-0003-3341-1378

Lei Zhou − *State Key Laboratory of Surface Physics and Department of Physics, Fudan University, Shanghai 200433, China; Key Laboratory of Micro and Nano Photonic Structures (MOE), Fudan University, Shanghai 200433, China*

Complete contact information is available at: https://pubs.acs.org/10.1021/acs.nanolett.2c03906

Author Contributions

Y.W. and Z.T. conceived the ideas and supervised the project. C.T. provided technical support. Q.H. and L.Z. supervised the theoretical work. S.W. and S.Z. conducted the terahertz measurements and data analysis. W.Q. and C.L. fabricated the metasurface samples. W.Q. and T.W. conducted the Kerr microscopy measurements and data analysis. S.W. and Y.L. conducted the terahertz-propagation and COMSOL simulations. S.W., W.Q., Y.W., and Z.T. wrote the manuscript. All the authors participated in the discussions.

Notes

The authors declare no competing financial interest.

■ ACKNOWLEDGMENTS

Z.T. and C.T. gratefully acknowledge the financial support by the National Key R&D Program of China (2021YFA1400202). Z.T., Y.W., L.Z., and C.T. gratefully acknowledge the funding support from the National Natural Science Foundation of China (12221004). Z.T., Y.W., and Q.H. acknowledge the support by the Shanghai Municipal Science and Technology Basic Research Project (22JC1400200). Z.T. acknowledges the funding support from the National Natural Science Foundation of China (12274091). Y.W. acknowledges the financial support by the National Key Research Program of China (2022YFA14033), the National Natural Science Foundation of China (Grant Nos. 11734006, 12274083, and 11974079) and the Shanghai Municipal Science and Technology Major Project (Grant No. 2019SHZDZX01). L.Z. acknowledges the support by the National Natural Science Foundation of China (62192771 and 11734007) and by the Shanghai Municipal Science and Technology Basic Research Project (20JC1414601). C.T. also acknowledges the support by the National Key Research and Development Program of China (2021YFA1400503).

■ REFERENCES

(1) Wang, Z.; Peng, Y.; Shi, C.; Wang, L.; Chen, X.; Wu, W.; Wu, X.; Zhu, Y.; Zhang, J.; Cheng, G.; Zhuang, S. Qualitative and Quantitative Recognition of Chiral Drugs Based on Terahertz Spectroscopy. *Analyst* **2021**, *146*, 3888−3898.

(2) Yang, X.; Zhao, X.; Yang, K.; Liu, Y.; Liu, Y.; Fu, W.; Luo, Y. Biomedical Applications of Terahertz Spectroscopy and Imaging. *Trends Biotechnol.* **2016**, *34*, 810−824.

(3) Smolyanskaya, O. A.; Chernomyrdin, N. V.; Konovko, A. A.; Zaytsev, K. I.; Ozheredov, I. A.; Cherkasova, O. P.; Nazarov, M. M.; Guillet, J. P.; Kozlov, S. A.; Kistenev, Y. V.; Coutaz, J. L.; Mounaix, P.; Vaks, V. L.; Son, J. H.; Cheon, H.; Wallace, V. P.; Feldman, Y.; Popov, I.; Yaroslavsky, A. N.; Shkurinov, A. P.; Tuchin, V. V. Terahertz Biophotonics as a Tool for Studies of Dielectric and Spectral Properties of Biological Tissues and Liquids. *Prog. Quantum Electron.* **2018**, *62*, 1−77.

(4) Jin, K. H.; Kim, Y.-G.; Cho, S. H.; Ye, J. C.; Yee, D.-S. High-Speed Terahertz Reflection Three-Dimensional Imaging for Nondestructive Evaluation. *Opt. Express* **2012**, *20*, 25432.

(5) Gowen, A. A.; O'Sullivan, C.; O'Donnell, C. P. Terahertz Time Domain Spectroscopy and Imaging: Emerging Techniques for Food Process Monitoring and Quality Control. *Trends Food Sci. Technol.* **2012**, *25*, 40−46.

(6) Ducournau, G.; Szriftgiser, P.; Pavanello, F.; Peytavit, E.; Zaknoune, M.; Bacquet, D.; Beck, A.; Akalin, T.; Lampin, J. F.; Lampin, J. F. THz Communications Using Photonics and Electronic Devices: The Race to Data-Rate. *J. Infrared, Millimeter, Terahertz Waves* **2015**, *36*, 198−220.

(7) Nagatsuma, T.; Ducournau, G.; Renaud, C. C. Advances in Terahertz Communications Accelerated by Photonics. *Nat. Photonics* **2016**, *10*, 371−379.

(8) Kampfrath, T.; Sell, A.; Klatt, G.; Pashkin, A.; Mährlein, S.; Dekorsy, T.; Wolf, M.; Fiebig, M.; Leitenstorfer, A.; Huber, R. Coherent Terahertz Control of Antiferromagnetic Spin Waves. *Nat. Photonics* **2011**, *5*, 31−34.

(9) Schlauderer, S.; Lange, C.; Baierl, S.; Ebnet, T.; Schmid, C. P.; Valovcin, D. C.; Zvezdin, A. K.; Kimel, A. V.; Mikhaylovskiy, R. V.; Huber, R. Temporal and Spectral Fingerprints of Ultrafast All-Coherent Spin Switching. *Nature* **2019**, *569*, 383−387.

(10) Li, X.; Qiu, T.; Zhang, J.; Baldini, E.; Lu, J.; Rappe, A. M.; Nelson, K. A. Terahertz Field−Induced Ferroelectricity in Quantum Paraelectric SrTiO3. *Science* **2019**, *364*, 1079−1082.

(11) Först, M.; Manzoni, C.; Kaiser, S.; Tomioka, Y.; Tokura, Y.; Merlin, R.; Cavalleri, A. Nonlinear Phononics as an Ultrafast Route to Lattice Control. *Nat. Phys.* **2011**, *7*, 854−856.

(12) Zaks, B.; Liu, R. B.; Sherwin, M. S. Experimental Observation of Electron-Hole Recollisions. *Nature* **2012**, *483*, 580−583.

(13) Danielson, J. R.; Lee, Y. S.; Prineas, J. P.; Steiner, J. T.; Kira, M.; Koch, S. W. Interaction of Strong Single-Cycle Terahertz Pulses with Semiconductor Quantum Wells. *Phys. Rev. Lett.* **2007**, *99*, 237401.

(14) Fleischer, S.; Zhou, Y.; Field, R. W.; Nelson, K. A. Molecular Orientation and Alignment by Intense Single-Cycle THz Pulses. *Phys. Rev. Lett.* **2011**, *107*, 163603.

(15) Choi, W. J.; Cheng, G.; Huang, Z.; Zhang, S.; Norris, T. B.; Kotov, N. A. Terahertz Circular Dichroism Spectroscopy of Biomaterials Enabled by Kirigami Polarization Modulators. *Nat. Mater.* **2019**, *18*, 820−826.

(16) GuerboukHa, H.; Nallappan, K.; Skorobogatiy, M. Toward Real-Time Terahertz Imaging. *Adv. Opt. Photonics* **2018**, *10*, 843−938.

(17) Monnai, Y.; Altmann, K.; Jansen, C.; Hillmer, H.; Koch, M.; Shinoda, H. Terahertz Beam Steering and Variable Focusing Using Programmable Diffraction Gratings. *Opt. Express* **2013**, *21*, 2347.

(18) Scherger, B.; Born, N.; Jansen, C.; Schumann, S.; Koch, M.; Wiesauer, K. Compression Molded Terahertz Transmission Blaze-Grating. *IEEE Trans. Terahertz Sci. Technol.* **2012**, *2*, 556−561.

(19) Squires, A. D.; Constable, E.; Lewis, R. A. 3D Printed Terahertz Diffraction Gratings And Lenses. *J. Infrared, Millimeter, Terahertz Waves* **2015**, *36*, 72−80.

(20) Esquius-Morote, M.; Gomez-Diaz, J. S.; Perruisseau-Carrier, J. Sinusoidally Modulated Graphene Leaky-Wave Antenna for Electronic Beamscanning at THz. *IEEE Trans. Terahertz Sci. Technol.* **2014**, *4*, 116−122.
(21) Tamagnone, M.; Capdevila, S.; Lombardo, A.; Wu, J.; Centeno, A.; Zurutuza, A.; Ionescu, A. M.; Ferrari, A. C.; Mosig, J. R.Graphene Reflectarray Metasurface for Terahertz Beam Steering and Phase Modulation. 2018, *arXiv:1806.02202*. arXiv.org e-Print archive. DOI: 10.48550/arXiv.1806.02202.
(22) Wu, J.; Shen, Z.; Ge, S.; Chen, B.; Shen, Z.; Wang, T.; Zhang, C.; Hu, W.; Fan, K.; Padilla, W.; Lu, Y.; Jin, B.; Chen, J.; Wu, P. Liquid Crystal Programmable Metasurface for Terahertz Beam Steering. *Appl. Phys. Lett.* **2020**, *116*, 131104.
(23) Liu, C. X.; Yang, F.; Fu, X. J.; Wu, J. W.; Zhang, L.; Yang, J.; Cui, T. J. Programmable Manipulations of Terahertz Beams by Transmissive Digital Coding Metasurfaces Based on Liquid Crystals. *Adv. Opt. Mater.* **2021**, *9*, 2100932.
(24) Cai, X.; Tang, R.; Zhou, H.; Li, Q.; Ma, S.; Wang, D.; Liu, T.; Ling, X.; Tan, W.; He, Q.; Xiao, S.; Zhou, L. Dynamically Controlling Terahertz Wavefronts with Cascaded Metasurfaces. *Adv. Photonics* **2021**, *3*, 036003.
(25) Yamada, I.; Takano, K.; Hangyo, M.; Saito, M.; Watanabe, W. Terahertz Wire-Grid Polarizers with Micrometer-Pitch Al Gratings. *Opt. Lett.* **2009**, *34*, 274.
(26) Ferraro, A.; Zografopoulos, D. C.; Missori, M.; Peccianti, M.; Caputo, R.; Beccherelli, R. Flexible Terahertz Wire Grid Polarizer with High Extinction Ratio and Low Loss. *Opt. Lett.* **2016**, *41*, 2009−2012.
(27) Shan, J.; Dadap, J. I.; Heinz, T. F. Circularly Polarized Light in the Single-Cycle Limit: The Nature of Highly Polychromatic Radiation of Defined Polarization. *Opt. Express* **2009**, *17*, 7431−7439.
(28) Masson, J.; Gallot, G. Terahertz Achromatic Quarter-Wave Plate. *Opt. Lett.* **2006**, *31*, 265−267.
(29) Jia, M.; Wang, Z.; Li, H.; Wang, X.; Luo, W.; Sun, S.; Zhang, Y.; He, Q.; Zhou, L. Efficient Manipulations of Circularly Polarized Terahertz Waves with Transmissive Metasurfaces. *Light Sci. Appl.* **2019**, *8*, 16.
(30) Jiang, Y.; Wang, L.; Wang, J.; Akwuruoha, C. N.; Cao, W. Ultra-Wideband High-Efficiency Reflective Linear-to-Circular Polarization Converter Based on Metasurface at Terahertz Frequencies. *Opt. Express* **2017**, *25*, 27616.
(31) Tian, H. W.; Shen, H. Y.; Zhang, X. G.; Li, X.; Jiang, W. X.; Cui, T. J. Terahertz Metasurfaces: Toward Multifunctional and Programmable Wave Manipulation. *Front. Phys.* **2020**, *8*, 584077.
(32) Wang, Z.; Li, S.; Zhang, X.; Feng, X.; Wang, Q.; Han, J.; He, Q.; Zhang, W.; Sun, S.; Zhou, L. Excite Spoof Surface Plasmons with Tailored Wavefronts Using High-Efficiency Terahertz Metasurfaces. *Adv. Sci.* **2020**, *7*, 2000982.
(33) Zang, X.; Yao, B.; Chen, L.; Xie, J.; Guo, X.; Balakin, A. V.; Shkurinov, A. P.; Zhuang, S. Metasurfaces for Manipulating Terahertz Waves. *Light Adv. Manuf.* **2021**, *2*, 10.
(34) Zhang, X.; Xu, Q.; Xia, L.; Li, Y.; Gu, J.; Tian, Z.; Ouyang, C.; Han, J.; Zhang, W. Terahertz Surface Plasmonic Waves: A Review. *Adv. Photonics* **2020**, *2*, 014001.
(35) Minerbi, E.; Keren-Zur, S.; Ellenbogen, T. Nonlinear Metasurface Fresnel Zone Plates for Terahertz Generation and Manipulation. *Nano Lett.* **2019**, *19*, 6072−6077.
(36) Luo, L.; Chatzakis, I.; Wang, J.; Niesler, F. B. P.; Wegener, M.; Koschny, T.; Soukoulis, C. M. Broadband Terahertz Generation from Metamaterials. *Nat. Commun.* **2014**, *5*, 3055.
(37) Polyushkin, D. K.; Hendry, E.; Stone, E. K.; Barnes, W. L. THz Generation from Plasmonic Nanoparticle Arrays. *Nano Lett.* **2011**, *11*, 4718−4724.
(38) Keren-Zur, S.; Tal, M.; Fleischer, S.; Mittleman, D. M.; Ellenbogen, T. Generation of Spatiotemporally Tailored Terahertz Wavepackets by Nonlinear Metasurfaces. *Nat. Commun.* **2019**, *10*, 1778.
(39) McDonnell, C.; Deng, J.; Sideris, S.; Ellenbogen, T.; Li, G. Functional THz Emitters Based on Pancharatnam-Berry Phase Nonlinear Metasurfaces. *Nat. Commun.* **2021**, *12*, 30.
(40) McDonnell, C.; Deng, J.; Sideris, S.; Li, G.; Ellenbogen, T. Terahertz Metagrating Emitters with Beam Steering and Full Linear Polarization Control. *Nano Lett.* **2022**, *22*, 2603−2610.
(41) Seifert, T.; Jaiswal, S.; Martens, U.; Hannegan, J.; Braun, L.; Maldonado, P.; Freimuth, F.; Kronenberg, A.; Henrizi, J.; Radu, I.; Beaurepaire, E.; Mokrousov, Y.; Oppeneer, P. M.; Jourdan, M.; Jakob, G.; Turchinovich, D.; Hayden, L. M.; Wolf, M.; Münzenberg, M.; Kläui, M.; Kampfrath, T. Efficient Metallic Spintronic Emitters of Ultrabroadband Terahertz Radiation. *Nat. Photonics* **2016**, *10*, 483−488.
(42) Kampfrath, T.; Battiato, M.; Maldonado, P.; Eilers, G.; Nötzold, J.; Mährlein, S.; Zbarsky, V.; Freimuth, F.; Mokrousov, Y.; Blügel, S.; Wolf, M.; Radu, I.; Oppeneer, P. M.; Münzenberg, M. Terahertz Spin Current Pulses Controlled by Magnetic Heterostructures. *Nat. Nanotechnol.* **2013**, *8*, 256−260.
(43) Yang, D.; Liang, J.; Zhou, C.; Sun, L.; Zheng, R.; Luo, S.; Wu, Y.; Qi, J. Powerful and Tunable THz Emitters Based on the Fe/Pt Magnetic Heterostructure. *Adv. Opt. Mater.* **2016**, *4*, 1944−1949.
(44) He, Q.; Sun, S.; Xiao, S.; Zhou, L. High-Efficiency Metasurfaces: Principles, Realizations, and Applications. *Adv. Opt. Mater.* **2018**, *6*, 1800415.
(45) Grady, N. K.; Heyes, J. E.; Chowdhury, D. R.; Zeng, Y.; Reiten, M. T.; Azad, A. K.; Taylor, A. J.; Dalvit, D. A. R.; Chen, H. T. Terahertz Metamaterials for Linear Polarization Conversion and Anomalous Refraction. *Science* **2013**, *340*, 1304−1307.
(46) Liu, C.; Wang, S.; Zhang, S.; Cai, Q.; Wang, P.; Tian, C.; Zhou, L.; Wu, Y.; Tao, Z. Active Spintronic-Metasurface Terahertz Emitters with Tunable Chirality. *Adv. Photonics* **2021**, *3*, 056002.
(47) Zutic, I.; Fabian, J.; Das Sarma, S. Spintronics: Fundamentals and Applications. *Rev. Mod. Phys.* **2004**, *76*, 323−410.
(48) Schulz, D.; Schwager, B.; Berakdar, J. Nanostructured Spintronic Emitters for Polarization-Textured and Chiral Broadband THz Fields. *ACS Photonics* **2022**, *9*, 1248−1255.
(49) Zdagkas, A.; McDonnell, C.; Deng, J.; Shen, Y.; Li, G.; Ellenbogen, T.; Papasimakis, N.; Zheludev, N. I. Observation of Toroidal Light Pulses. *Nat. Photonics* **2022**, *16*, 523−528.
(50) Zhu, B.; Fu, Z.; Chen, Y.; Peng, S.; Jin, C.; Fan, G.; Zhang, S.; Wang, S.; Tian, C.; Wang, Y.; Kapteyn, H.; Murnane, M.; Tao, Z. Spatially Homogeneous Few-Cycle Compression of Yb Lasers via All-Solid-State Free-Space Soliton Management. *Opt. Express* **2022**, *30*, 2918−2932.
(51) Zhang, S.; Fu, Z.; Zhu, B.; Fan, G.; Chen, Y.; Wang, S.; Liu, Y.; Baltuska, A.; Jin, C.; Tian, C.; Tao, Z. Solitary Beam Propagation in Periodic Layered Kerr Media Enables High-Efficiency Pulse Compression and Mode Self-Cleaning. *Light Sci. Appl.* **2021**, *10*, 53.
(52) Planken, P. C. M.; Nienhuys, H.-K.; Bakker, H. J.; Wenckebach, T. Measurement and Calculation of the Orientation Dependence of Terahertz Pulse Detection in ZnTe. *J. Opt. Soc. Am. B* **2001**, *18*, 313.
(53) Leitenstorfer, A.; Hunsche, S.; Shah, J.; Nuss, M. C.; Knox, W. H. Detectors and Sources for Ultrabroadband Electro-Optic Sampling: Experiment and Theory. *Appl. Phys. Lett.* **1999**, *74*, 1516−1518.
(54) Battiato, M.; Carva, K.; Oppeneer, P. M. Superdiffusive Spin Transport as a Mechanism of Ultrafast Demagnetization. *Phys. Rev. Lett.* **2010**, *105*, 027203.
(55) Cao, W. N.; Li, J.; Chen, G.; Zhu, J.; Hu, C. R.; Wu, Y. Z. Temperature-Dependent Magnetic Anisotropies in Epitaxial Fe/CoO/MgO(001) System Studied by the Planar Hall Effect. *Appl. Phys. Lett.* **2011**, *98*, 262506.
(56) Qiu, H.; Zhou, L.; Zhang, C.; Wu, J.; Tian, Y.; Cheng, S.; Mi, S.; Zhao, H.; Zhang, Q.; Wu, D.; Jin, B.; Chen, J.; Wu, P. Ultrafast Spin Current Generated from an Antiferromagnet. *Nat. Phys.* **2021**, *17*, 388−394.
(57) Liu, C. Q.; Lu, W.-T.; Wei, Z. X.; Miao, Y. F.; Wang, P.; Xia, H.; Liu, Y. P.; Zeng, F. L.; Zhang, J. R.; Zhou, C.; Zhao, H. B.; Wu, Y.

Z.; Yuan, Z.; Qi, J. Strain-Induced Anisotropic Terahertz Emission From a Fe(211)/Pt(110) Bilayer. *Phys. Rev. Appl.* **2021**, *15*, 044022.
(58) Zhou, C.; Liu, Y. P.; Wang, Z.; Ma, S. J.; Jia, M. W.; Wu, R. Q.; Zhou, L.; Zhang, W.; Liu, M. K.; Wu, Y. Z.; Qi, J. Broadband Terahertz Generation via the Interface Inverse Rashba-Edelstein Effect. *Phys. Rev. Lett.* **2018**, *121*, 086801.
(59) Kryder, B. M. H.; Gage, E. C.; Mcdaniel, T. W.; Challener, W. A.; Rottmayer, R. E.; Ju, G.; Hsia, Y.; Erden, M. F. Heat Assisted Magnetic Recording. *Proc. IEEE* **2008**, *96*, 1810−1835.
(60) Gueckstock, O.; Nádvorník, L.; Seifert, T. S.; Borchert, M.; Jakob, G.; Schmidt, G.; Woltersdorf, G.; Kläui, M.; Wolf, M.; Kampfrath, T. Modulating the Polarization of Broadband Terahertz Pulses from a Spintronic Emitter at Rates up to 10 kHz. *Optica* **2021**, *8*, 1013.

https://doi.org/10.1021/acs.nanolett.2c03906
Nano Lett. 2022, 22, 10111−10119